Effect of summer Arctic sea ice on the reverse August precipitation anomaly in eastern China between 1998 and 2016

Both 1997/1998 and 2015/2016 saw super El Niño events on record. Meanwhile, the peak intensity and decay conditions of the two super episodes are similar. The total rainfall in eastern China during the summers of 1998 and 2016 increase remarkably as expected. Additionally, the June and July rainfall anomalies in 1998 and 2016 also exhibit many similarities under the influence of the similar super El Niño events, which is reasonable according to the previous studies. However, the August precipitation anomalies between the two years show nearly reverse patterns (Fig. 1). The mechanism of the reverse August precipitation anomalies over eastern China between 1998 and 2016 under similar El Niño conditions is investigated in this study.

The August precipitation anomalies in 1998 and 2016 exhibit a dipole pattern but with opposite sign over eastern China, i.e. notable increasing/decreasing over central China (approximately 30°−35°N) and decreasing/increasing over southeastern China (approximately south of 25°N) (Fig. 1). Statistical analyses reveal that such a dipole rainfall pattern over eastern China in August is concurrent with pronounced sea ice concentration (SIC) anomalies over the Barents-Kara Seas (BKS) in July and August (Figs. 2a and 2b). Therefore, a July sea ice area index (SIAI) is defined to diagnose the potential influence of sea ice on the precipitation over eastern China (Fig. 2c). It is found that with regard to the reduced SIA in July over the BKS, the thermal condition of the underlying surface changes. The positive sea surface temperature anomaly in the polar region stimulates significant divergence anomaly at the upper troposphere, which leads to the rotational component and the vorticity generation. Consequently, anomalous upper-level convergence emerges over the Caspian Sea. The advections of vorticity anomaly by the anomalous divergent and convergent flow act as effective Rossby wave sources and apparent Rossby wave sources emerge near the Caspian Sea (Fig. 3). As a result, a Rossby wave train propagates from the Caspian Sea eastward to East Asia (Fig. 4). Due to the eastward propagation of the Rossby wave activity, significantly positive barotropic and baroclinic energy conversion occurs in the jet-exit region near Korea in August, which resembles well the composited anomalies associated with the Pacific-Japan (PJ) pattern (Fig. 5). It implies that the perturbation energy accumulation in East Asia stimulates the formation of the PJ pattern, which favors the dipole rainfall anomaly pattern over eastern China.

Numerical experiments are employed to verify the results of the observational analyses (Fig. 6). As indicated by the model results, associated with the reduced sea ice over the BKS, significant anomalous cyclone and anticyclone appear in August in the subtropical western Pacific and near Korea-Japan, respectively. Meanwhile, the spatial pattern of the simulated height anomalies over Korea-Japan and the western Pacific resembles the PJ pattern that is identified by the regressing onto the July SIAI. Therefore, both observational and numerical analyses suggest that the sea ice anomaly over the BKS may modulate the atmospheric circulation and precipitation in eastern China during August.

The spatial distribution of the observed rainfall anomaly over eastern China and the anomalous large-scale atmospheric circulation in August 2016 (1998) largely resemble (mirror) the regressed ones with regard to the July SIAI over the BKS. Thus, the observed positive (negative) SIA anomaly over the BKS in August 1998 (2016) suggests the potential contribution of the upstream sea ice to the reverse August precipitation anomalies in eastern China between 1998 and 2016 synchronizing with strong El Niño events.

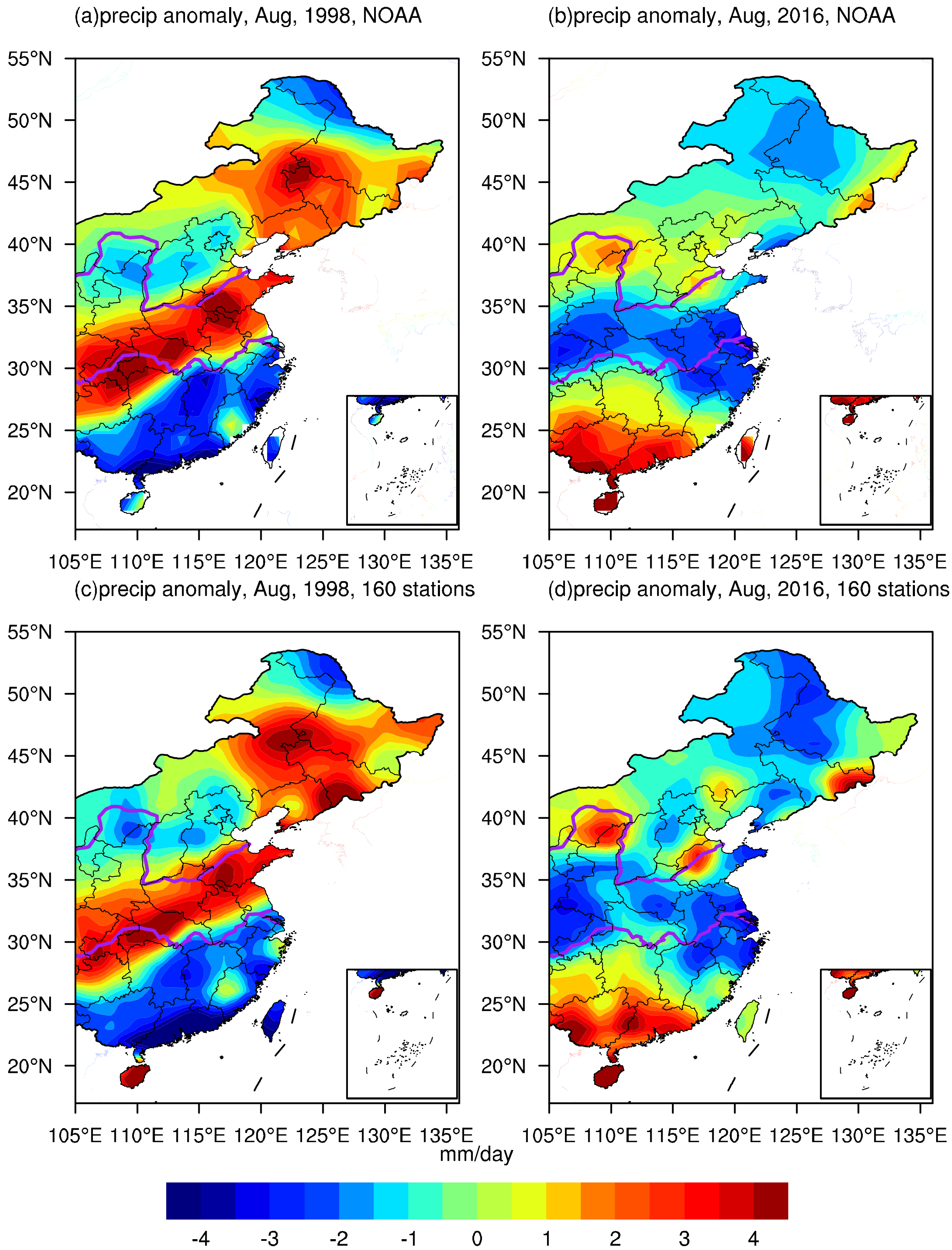

Fig. 1 Distribution of August precipitation anomalies (units: mm/day) in China east of 105 °E during 1998 (a, c) and 2016 (b, d). (a, b) Data from NOAA, (c, d) data provided by 160 stations from the China Meteorological Administration.

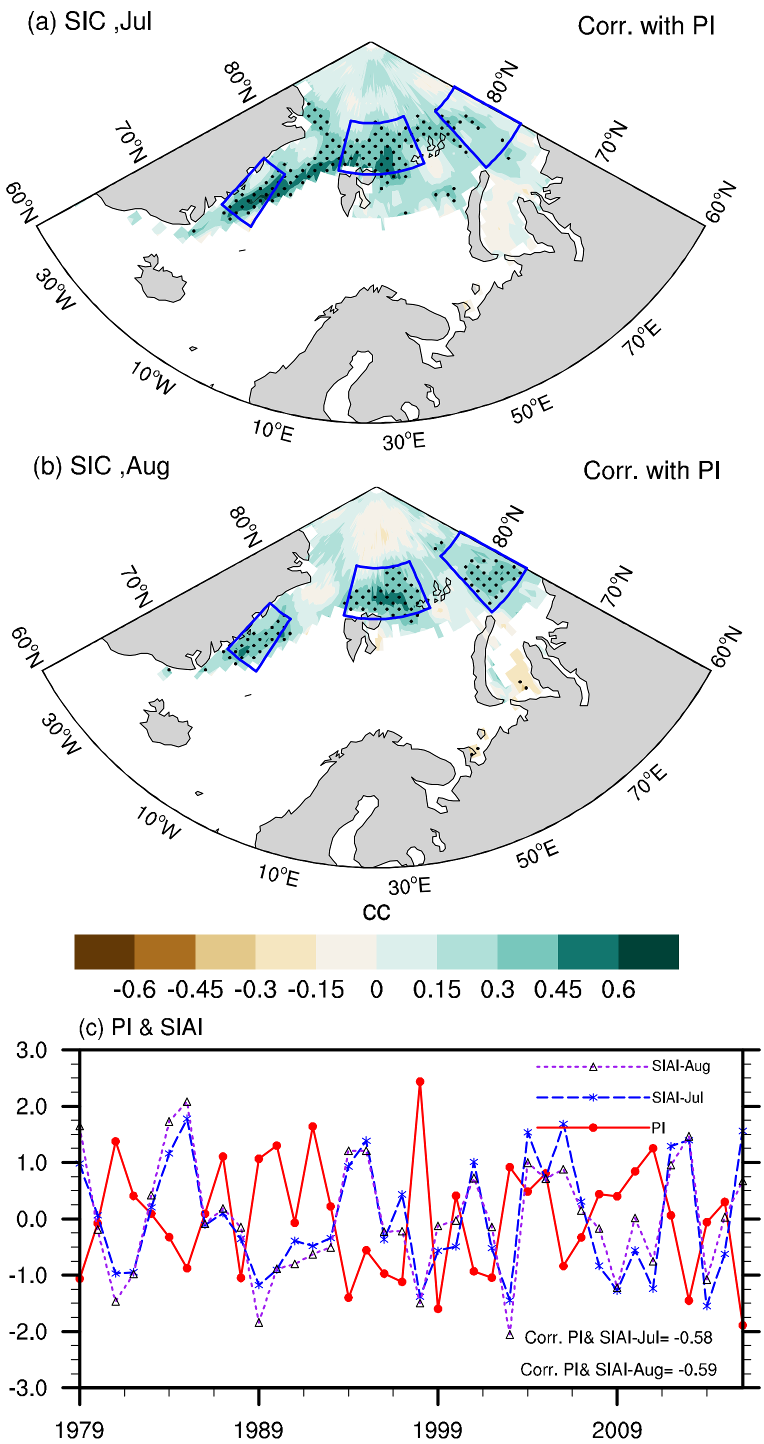

Fig. 2 Correlation maps of sea ice concentration in (a) July and (b) August with regard to the August PI during 1979–2016. Stippled values are significant at the 90% confidence level, based on the Student's *t* test. (c) Normalized time series of the August PI and SIAI of July and August; the correlation coefficients are given in the lower right corner.

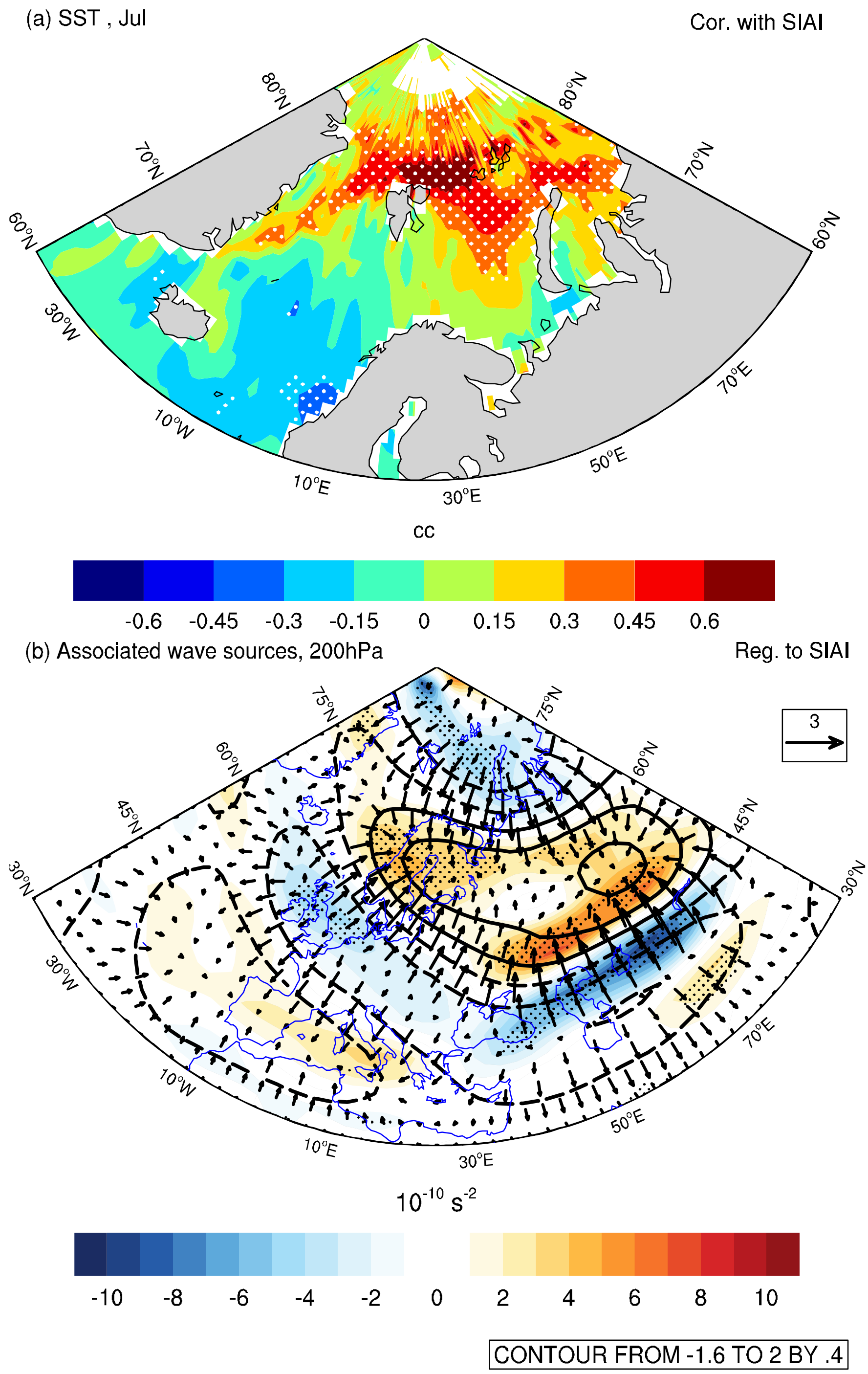

Fig. 3 Correlation maps of (a) the SSTA (units: ℃), (b) Rossby wave sources (shading, units: s^{-2}), velocity potential (contour, units: $m^2\ s^{-1}$), and divergent wind (vector, units: $m\ s^{-1}$) at 200-hPa in July with the July SIAI during 1979-2016. Stippled values are significant at the 90% confidence level, based on the Student's *t* test.

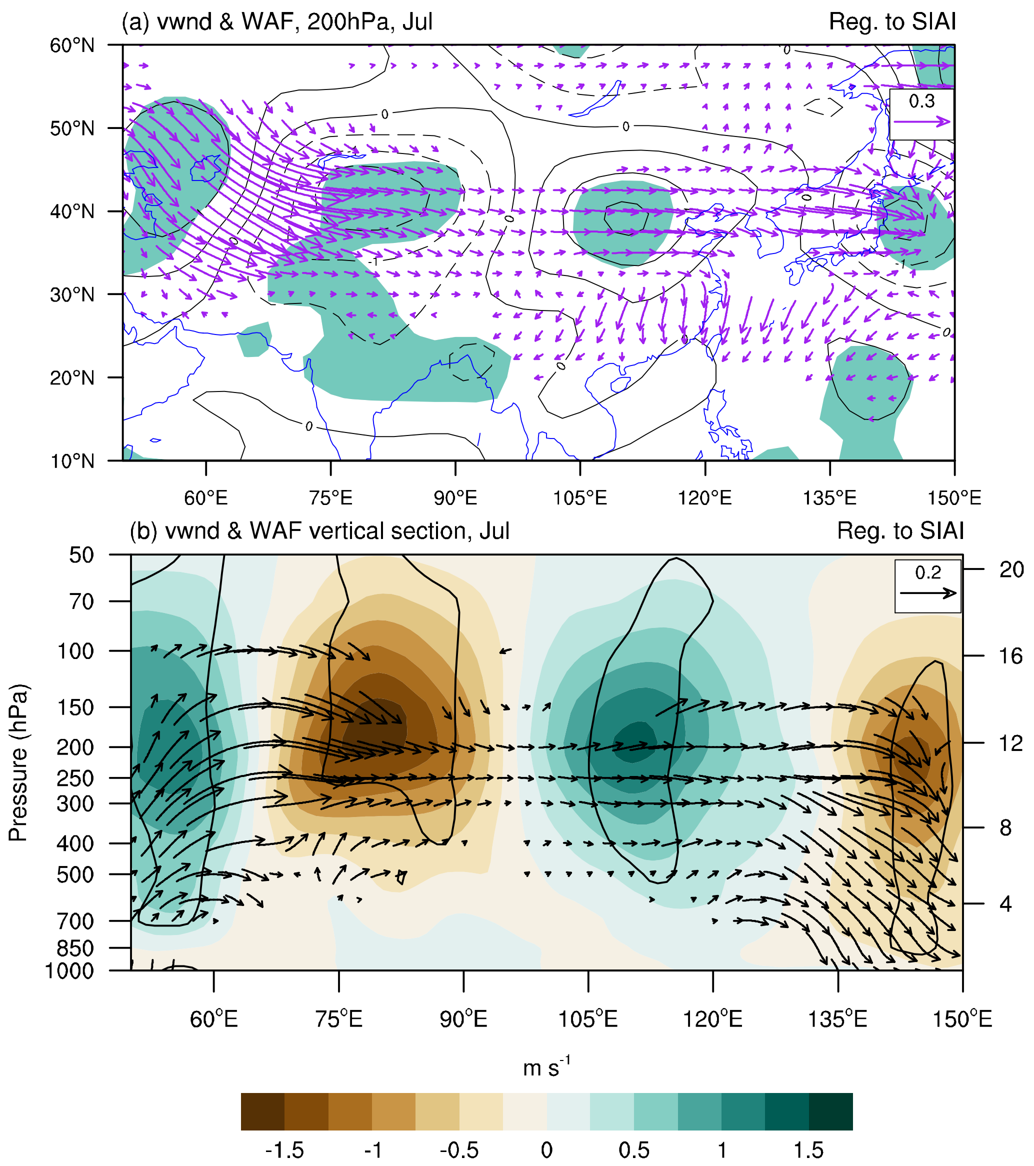

Fig. 4 Regression maps of (a) the July meridional wind (contour, units: m s^{-1}) and horizontal wave activity flux (vector, units: m^2 s^{-2}) at 200-hPa, (b) the vertical–zonal cross section averaged along 35 °–45 °N for the wave activity flux (vector, units: m^2 s^{-2}) and meridional wind anomalies (shading; units: m s^{-1}) with regard to the July SIAI during 1979-2016. Shading regions in (a) and regions enclosed by contours in (b) indicate that the meridional wind anomalies are significant at the 90% confidence level, based on the Student's *t* test.

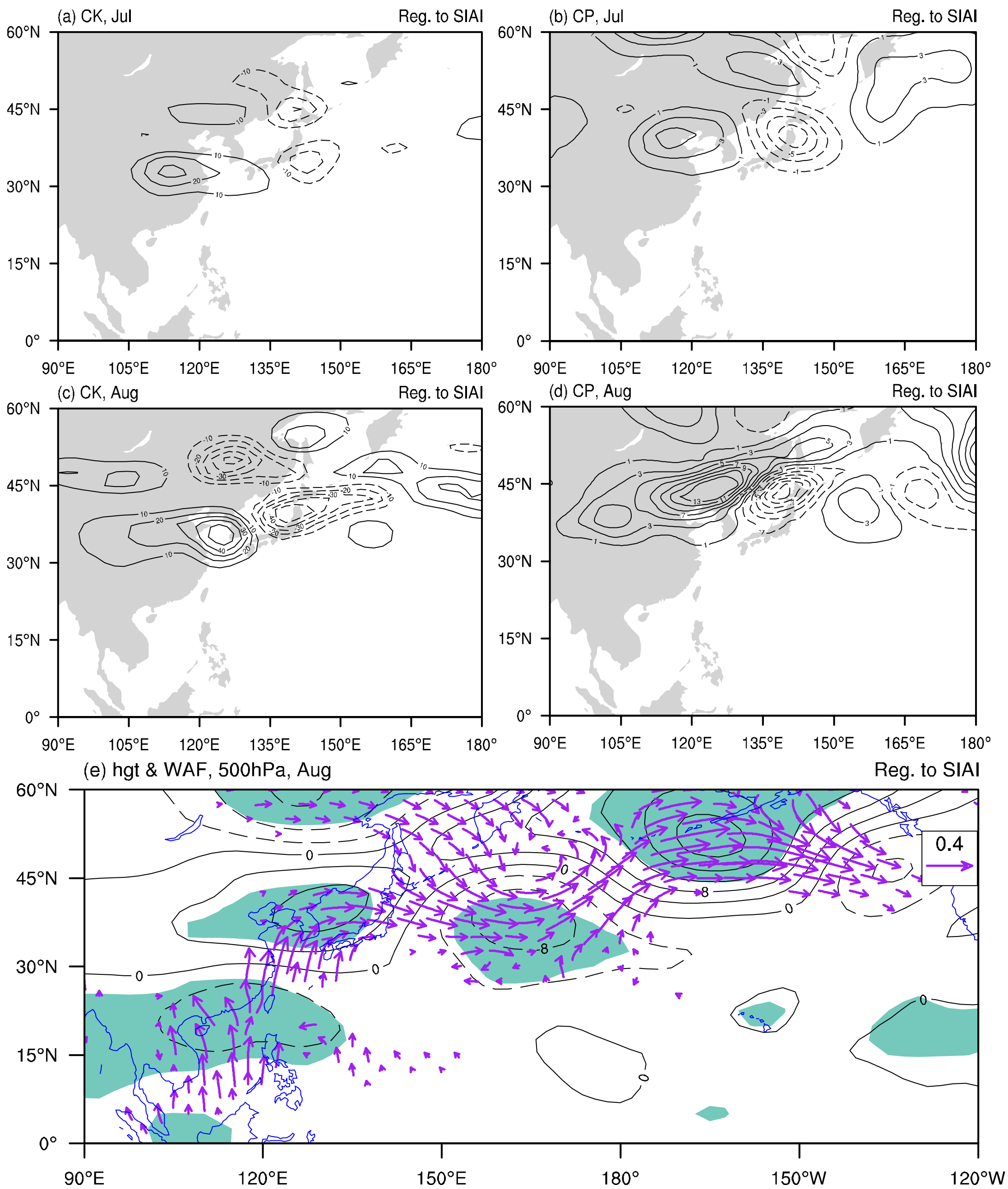

Fig. 5 Regression maps of (a) local barotropic energy conversion (units: 10^{-6} m^2s^{-3}) at 200-hPa and (b) vertically integrated baroclinic energy conversion (units: 10^{-3} Wm^{-2}) in July with regard to the July SIAI during 1979-2016. (c) and (d) same as (a) and (b), but for August. (e) 500-hPa wave activity flux (vector, units: m^2 s^{-2}) and geopotential height (contours, units: gpm) in August with regard to the July SIAI during 1979-2016, shading values are significant at the 90% confidence level, based on the Student's *t* test.

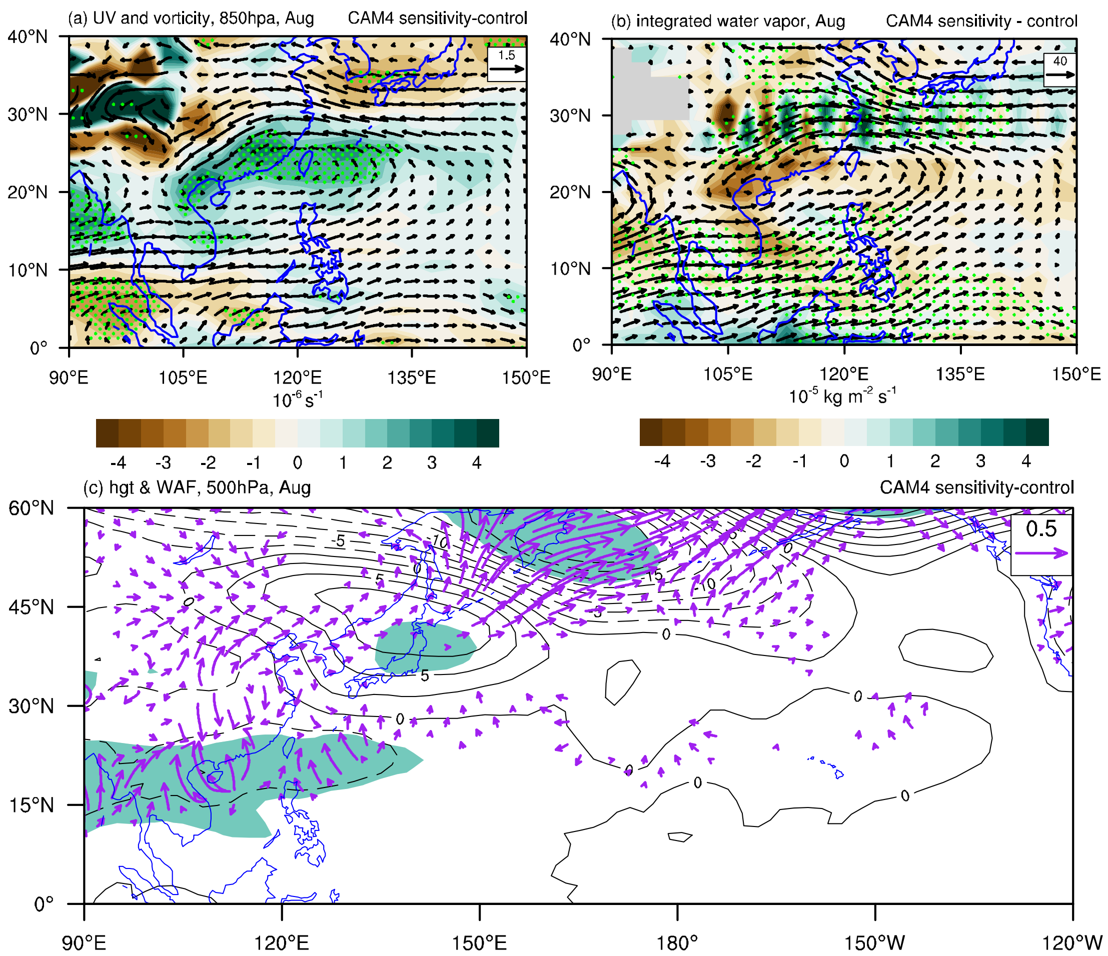

Fig. 6 The difference between the sensitivity and control run in CAM4 of the August (a) 850-hPa wind (vector; units: m s^{-1}) and vorticity (shaded, units: 10^{-6} s^{-1}), (b) vertically integrated water vapor vectors (units: kg m^{-1} s^{-1}) and water vapor flux divergence (shading, units: 10^{-5} kg m^{-2} s^{-1}), (c) 500-hPa geopotential height (contours, units: gpm) and the associated wave activity flux (vector, units: m^{2} s^{-2}). Values stippled in (a, b) and shaded in (c) are significant at the 90% confidence level, based on the Student's *t* test.